The roles of a flagellar HSP40 ensuring rhythmic beating

Xiaoyan Zhu[a,†,‡], Emiliya Poghosyan[b,†], Lenka Rezabkova[b], Bridget Mehall[a], Hitoshi Sakakibara[c], Masafumi Hirono[d], Ritsu Kamiya[e], Takashi Ishikawa[b], and Pinfen Yang[a,*]

[a]Department of Biological Sciences, Marquette University, Milwaukee, WI 53233; [b]Laboratory of Biomolecular Research, Division of Biology and Chemistry, Paul Scherrer Institute, 5232 Villigen PSI, Switzerland; [c]National Institute of Information and Communications Technology (NICT), Advanced ICT Research Institute, Hyogo 651-2492, Japan; [d]Department of Frontier Bioscience, Hosei University, Tokyo 184-8584, Japan; [e]Department of Life Science, Faculty of Science, Gakushuin University, Tokyo 171-8588, Japan

ABSTRACT **HSP40s are regarded as cochaperones, perpetually shuttling client polypeptides to HSP70s for refolding. However, many HSP40s that are central for disparate processes diverge from this paradigm. To elucidate the noncanonical mechanisms, we investigated HSP40 in the radial spoke (RS) complex in flagella. Disruption of the gene by the MRC1 transposon in *Chlamydomonas* resulted in jerky flagella. Traditional electron microscopy, cryo-electron tomography, and sub-tomogram analysis revealed RSs of various altered morphologies that, unexpectedly, differed between the two RS species. This indicates that HSP40 locks the RS into a functionally rigid conformation, facilitating its interactions with the adjacent central pair apparatus for transducing locally varied mechanical feedback, which permits rhythmic beating. Missing HSP40, like missing RSs, could be restored in a tip-to-base direction when HSP40 mutants fused with a HSP40 donor cell. However, without concomitant de novo RS assembly, the repair was exceedingly slow, suggesting HSP40/RS-coupled intraflagellar trafficking and assembly. Biochemical analysis and modeling uncovered spoke HSP40's cochaperone traits. On the basis of our data, we propose that HSP40 accompanies its client RS precursor when traveling to the flagellar tip. Upon arrival, both refold in concert to assemble into the mature configuration. HSP40's roles in chaperoning and structural maintenance shed new light on its versatility and flagellar biology.**

Monitoring Editor
Wallace Marshall
University of California, San Francisco

Received: Jan 19, 2018
Revised: Oct 12, 2018
Accepted: Nov 9, 2018

INTRODUCTION

Heat shock protein (HSP)40s (J proteins) and HSP70s constitute a ubiquitous chaperone system that facilitates polypeptide folding in both prokaryotes and eukaryotes (reviewed by Kampinga and Craig, 2010). Yet HSP40 genes in each eukaryotic organism greatly outnumber HSP70 genes. For example, in the Phytozome database (https://phytozome.jgi.doe.gov/pz/portal.html) nearly 70 *Chlamydomonas reinhardtii* genes are annotated as DnaJ-like or encoding a DnaJ domain, the signature of the HSP40/DnaJ family. In contrast, there are only 13 HSP70-like genes. Although one HSP70 could partner with several HSP40s, it is becoming clear that this ancestral partnership is not obligatory (Ajit Tamadaddi and Sahi, 2016). A number of HSP40 isoforms—such as those specific to motile cilia and flagella (Yang *et al.*, 2008), to spliceosomes (Pandit *et al.*, 2009), and for suppressing protein aggregations

This article was published online ahead of print in MBoC in Press (http://www.molbiolcell.org/cgi/doi/10.1091/mbc.E18-01-0047) on November 14, 2018.

†These authors contributed equally to this work.

‡Present address: Department of Biochemistry and Molecular Genetics, Northwestern University Feinberg School of Medicine, Chicago, IL 60611.

*Address correspondence to: Pinfen Yang (Pinfen.yang@marquette.edu).

Abbreviations used: 1D, one-dimensional; 3D, three-dimensional; a.a., amino acids; AH, amphipathic helix; CP, central pair; D, donor; EM, electron microscopy; EMDB, Electron Microscopy Data Bank; ET, electron tomography; GFP, green fluorescent protein; HSP, heat shock protein; IFT, intraflagellar transport; LTR, long terminal repeat; NDK, nucleoside diphosphate kinase; NG, Neongreen; Ni-NTA, nickel-nitrilotriacetic acid; PDB, Protein Data Bank; PMM, paromomycin; R, receiver; RNAi, RNA interference; RS, radial spoke; RSP, radial spoke protein; TAP, Tris-acetate-phosphate; TEV, tobacco etch virus; UV, ultraviolet; WT, wild type.

(Hageman *et al.*, 2010; Ito *et al.*, 2016)—likely operate in an HSP70-independent manner. It is unclear how HSP40s, equipped to deliver various polypeptides and to activate the ATPase activity of HSP70s, are harnessed for other purposes. Elucidation of the noncanonical mechanisms may enlighten the wide spectrum of HSP40-mediated critical reactions.

Flagella of the green alga *Chlamydomonas* harbor an HSP40 and an HSP70 (Pazour *et al.*, 2005; Silflow *et al.*, 2011). They beat with the typical 9+2 axoneme, which consists of a ring of 9 microtubule outer doublets encircling the central pair (CP) apparatus with two microtubule singlets. These microtubules associate with a multitude of molecular complexes, such as dynein motors, radial spokes (RSs), and CP projections, each at a precise position in a 96-nm unit that repeats throughout the length of the axoneme. HSP40 and HSP70, respectively, reside in RSs and the CP that constitute a mechanical feedback system to enable rhythmic beating (Mitchell *et al.*, 2005; Satouh *et al.*, 2005; Yang *et al.*, 2005). HSP70 may be also enriched at the tip of flagella (Bloch and Johnson, 1995).

However, at present, accumulated evidence suggests that spoke HSP40 (alias: RSP16) and HSP70 operate independently. Spoke HSP40 is a type II DnaJ. Although all its orthologues have a DnaJ or J domain known for activation of HSP70's ATPase activity, the histidine-proline-aspartic acid tripeptide requisite for ATPase activation are not strictly conserved (Yang *et al.*, 2005). RNA interference (RNAi)-based HSP40 depletion resulted in immotile cells with jerky flagella (Yang *et al.*, 2008). Motility was restored almost immediately upon electroporation of recombinant HSP40 with or, surprisingly, without the J domain. Finally, the *Chlamydomonas* mutant defective in the *HSP70* gene still generates full-length motile flagella (Silflow *et al.*, 2011) indicative of functional RSs.

Compared with other radial spoke proteins (RSPs), spoke HSP40 is unusual. Axonemal components are imported from the cell body and then assemble at the microtubule plus ends at the flagellar tip (Rosenbaum and Child, 1967; Johnson and Rosenbaum, 1992; Lechtreck *et al.*, 2018). In general, components in an axonemal complex are first packaged into a precursor complex in the cell body (Fowkes and Mitchell, 1998; Qin *et al.*, 2004) and then delivered by anterograde intraflagellar transport (IFT) trains to the tip for the final assembly (reviewed by Rosenbaum and Witman, 2002). Yet mature and precursor RSs appear rather different in several ways. In contrast to 20S Y-shaped mature RSs, RS precursors sediment as 12S Γ-shaped particles (Yang *et al.*, 2001; Qin *et al.*, 2004; Diener *et al.*, 2011), lacking HSP40 (Yang *et al.*, 2005) and the signature bifurcated neck, where HSP40 is predicted to reside (Pigino *et al.*, 2011; Zhu *et al.*, 2017b). It is unclear whether HSP40 dissociates from RS precursors during in vitro fractionation or travels independently before joining the neck region. HSP40's effect on RSs appears to be subtle at best. Even though HSP40 depletion causes jerky flagella, the only detectable abnormality is deformation of a few RSs in many thin-section electron micrographs (Yang *et al.*, 2008). Because the harsh procedures of this traditional method may alter structures of biological samples (Lucic *et al.*, 2013), independent approaches are needed to reveal the exact defects of HSP40-minus RSs and the roles of this HSP40 isoform consigned specifically to RSs.

This study investigates a new *Chlamydomonas* HSP40 mutant, *pf33*, which inspires new approaches and in-depth analyses. The results support models proposing how an HSP40 dimer is conscripted to couple RS trafficking and assembly as a chaperone independent of HSP70 and then to stabilize mature RSs to confer rhythmic beating of motile flagella.

RESULTS

Discovery of an HSP40 transposon insertional mutant

An ultraviolet (UV) mutagenesis project (Kamiya, 1988) recovered a candidate HSP40 mutant, *pf33*. Like HSP40 RNAi cells, most *pf33* cells had jerky flagella, even though a few swam like wild-type (WT) cells. Swimmers remained despite isolation of single clones and backcrosses. Western blot analysis showed that HSP40 was indeed diminished in *pf33* axonemes, whereas the other representative RS proteins (RSPs) appeared normal (Figure 1A). The positive and negative controls were from the WT strain and the spokeless *pf14* mutant. Protein stain of a duplicated membrane demonstrated similar protein loads (bottom panel). Thin-section electron microscopy (EM) showed that, contrary to the mostly Y-shaped RSs (arrows in Figure 1B) in WT axonemes (top panel), many RSs in *pf33* axonemes appeared deformed (bottom panel, arrowheads). While the deformation was more evident than that of the RNAi strain processed by a different method, it was similar to that in primary cilia dyskinesia patients with a defective HSP40 gene (El Khouri *et al.*, 2016).

To test whether *pf33* was an HSP40 mutant, we PCR-amplified the gene as overlapping fragments (Figure 1C). The 5′ fragments (represented by fragment 2) amplified from the genomic DNA of *pf33* and WT cells were identical, whereas the downstream fragment 3 and fragment 4 from *pf33* were 1.3 kb longer (Figure 1D, left panel). Restriction digest (right panel) predicted additional sequences near the stop codon. Sequencing of the two longer fragments using primer 3AS and 4S, respectively, revealed the sequence of the MRC1 transposon inserted 37 base pairs downstream to the stop codon in a reverse orientation. The 3′ long terminal repeat (LTR) was 272 base pairs shorter, perhaps lost during insertion or due to decay afterward (Kim *et al.*, 2006; Gallaher *et al.*, 2015). Curiously, the insertion site did not have the 5-base pair target-site sequence. Thus MRC1's target-site sequence is not absolute. MRC1 translocation into *pf33*'s HSP40 gene may be triggered by UV illumination during mutagenesis (Kim *et al.*, 2006). The natural MRC1 retranslocation (Mayfield *et al.*, 1987; Gallaher *et al.*, 2015) may account for a few swimmers in liquid cultures of *pf33* subclones. HSP40 proteins in *pf33* axoneme preparations (Figure 1A) could come from these swimmers or incomplete block of gene expression by the transposon at the 3′ untranslated region.

Cryo–electron tomography revealed restricted structural defects in *pf33* RSs

To examine the structural impact from missing spoke HSP40, we have explored several methods. Cryo–electron tomography (cryo-ET) and sub-tomogram averaging based on the 96-nm repeating unit (Figure 2) provide the highest resolution for the in situ structures. The final average of the transverse section through the second RS (RS2) (Figure 2, A–C) and the longitudinal section (Figure 2, D–F) show relatively weak density in spokehead and spokeneck regions of the *pf33* axoneme (Figure 2, B and E) compared with other parts of the spoke as well as the WT control structure (Figure 2, A and D). In contrast, the density is completely missing in the structure of the *pf24* mutant, which has severe deficiencies in head and neck proteins, including HSP40 (Figure 2, C and F). The estimated resolution of three-dimensional (3D) reconstruction for Figure 2, B and E, is 4.4 nm, as shown by the representative Fourier shell correlation plots (Supplemental Figure S1). This means that the head and neck parts of *pf33* RSs are structurally heterogeneous or flexible. This, in conjunction with an abundance of all spoke proteins except HSP40 in the *pf33* axoneme (Figure 1A), indicates that, in the absence of HSP40, the majority of the spokes assembled the head and neck, but the structures are abnormal.

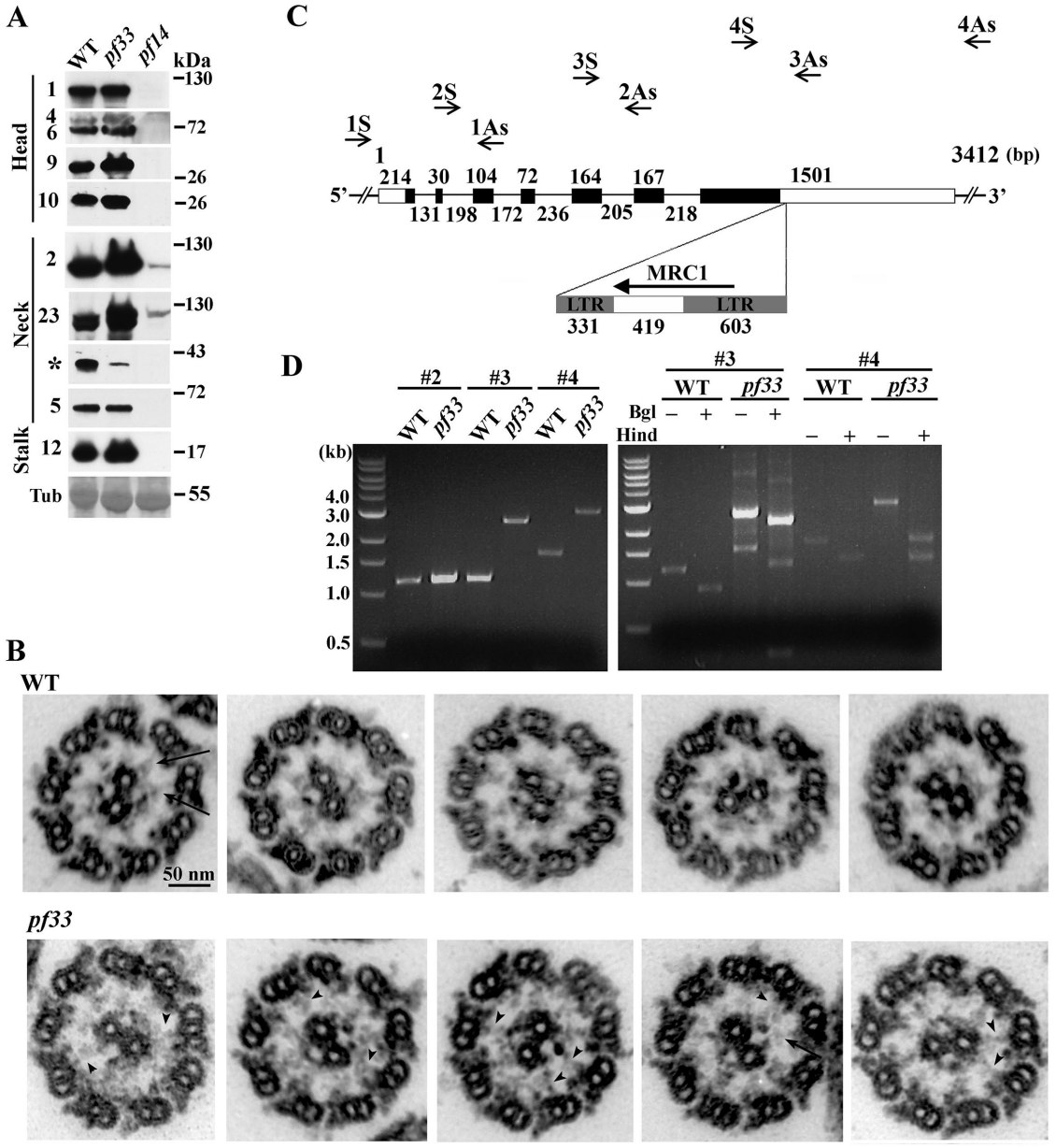

FIGURE 1: Characterization of a new HSP40 mutant, *pf33*. (A) Western blots show a specific HSP40 deficiency (asterisk) in *pf33* axonemes. The other proteins located at three major areas of the RS appear normal. Tubulin bands in the Ponceau S–stained membrane (bottom panel) show the protein loads. The WT strain serves as a positive control. The spokeless strain *pf14* is a negative control. (B) Electron micrograph of axoneme cross-sections. Nearly all 45 RSs in all 5 collected WT axoneme sections (top panel) appear to be typical Y-shaped complexes (arrows), rendering an ordered appearance of axonemes. In contrast, the RSs in five images representing 12 focused *pf33* axoneme sections appear disordered (bottom panel). The head/neck region of some RSs appears split or tilted (arrowhead). Only one seems normal (arrow). (C) A schematic depicting the *HSP40* gene, the PCR genotyping strategy, and a partial MRC1 transposon inserted downstream of the stop codon in the reverse direction in *pf33*'s *HSP40* gene. The primer pairs for PCR are depicted on arrows. The base pair number of each segment is indicated above or below. (D) DNA gels of PCR products from WT and *pf33* cells (left) and restriction digest (right). PCR fragments of the N-terminal region from both strains are identical (e.g., the #2 fragment amplified by the primer pair 2S and 2AS). But fragments #3 and #4 from *pf33* are 1.3 kb larger than those from the WT. The two fragments overlapped at the region around the stop codon. *Bgl*II and *Hin*dIII digests demonstrate specific PCR amplification. Sequencing of fragments #3 and #4 showed that the additional sequence is a partial 1.3-kb MRC1 fragment. The 3′ LTR is truncated.

Different structural defects in two RS populations in *pf33*

Interestingly enough, defects in RS1 and RS2 that are anchored near distinct inner dynein arms are not identical in *pf33* axonemes (Figure 3). The comparison between transverse sections of WT and *pf33* shows a density missing in one of the two neck branches of only *pf33* RS1, as well as overall weaker spokehead density in this RS1 (compare red arrows in Figure 3, A and C). *pf33*'s RS2 (Figure 3D) has weaker spokehead and spokeneck densities compared with the WT control (Figure 3B). The plane sectioned through RS2 in Figures 2 and 3 is illustrated in Figure 3E.

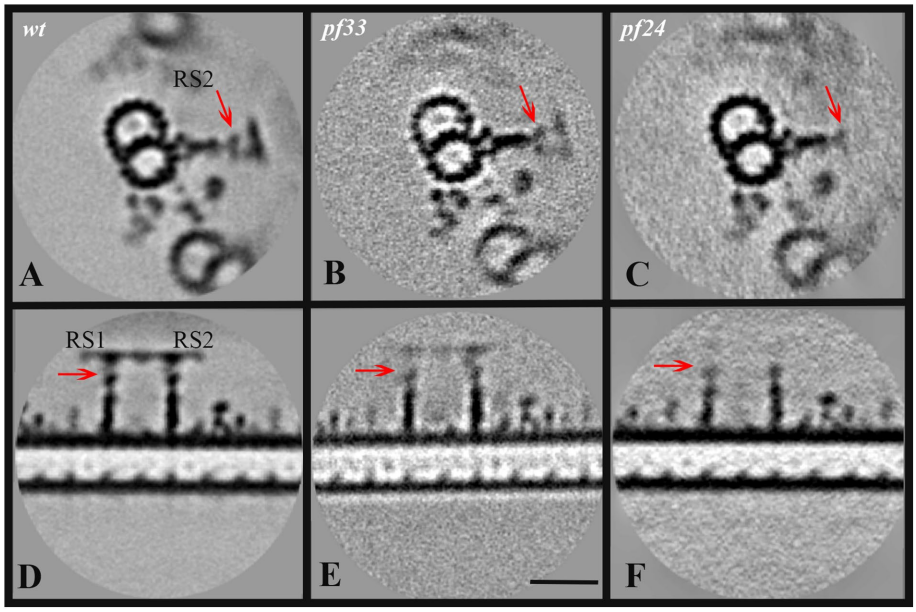

FIGURE 2: Structural comparison of RSs from the WT (A, D) (EMD-2131; Bui *et al.*, 2012), *pf33* (B, E), and *pf24* (C, F; Pigino *et al.*, 2011) *Chlamydomonas* strain in cryo-electron tomograms. Density maps from averaged sub-tomograms of the 96-nm periodic unit are represented as transverse sections at the RS2 level (A–C) and longitudinal sections (D–F). The major differences among these three strains are at the neck (red arrow) and head regions. The density at these regions is weak and blurred for *pf33* (B, E) as compared with WT (A, D); however, it is not completely lost, as in the headless strain *pf24* (C, F). Scale bar: 24 nm.

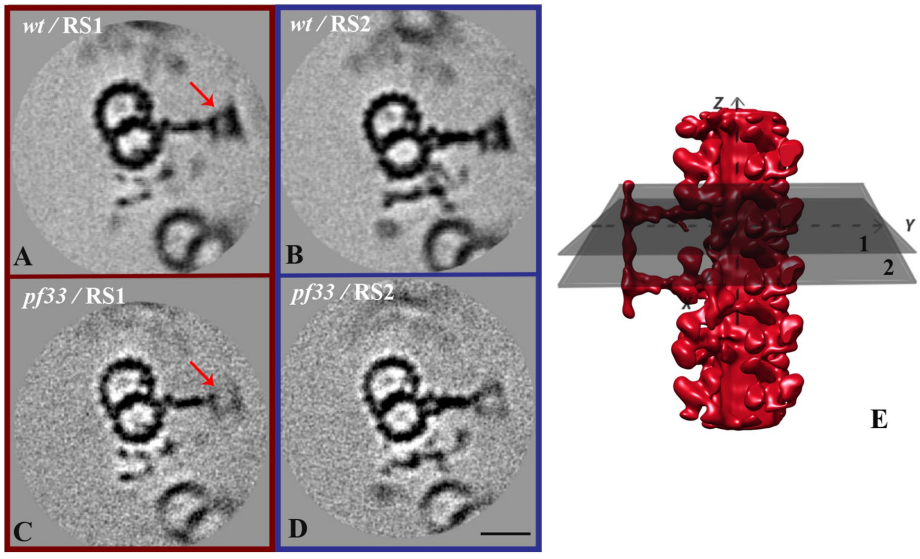

FIGURE 3: Structural comparison between RS1 (A, C) and RS2 (B, D) of the WT (A, B) and *pf33* (C, D) *Chlamydomonas*. (E) Schematic diagram illustrating the corresponding planes, crossing RS2 in the 96-nm periodic unit of *C. reinhardtii* flagella (*EMDB 1941*), of averaged slices shown in Figures 2 (plane 1) and 3 (plane 2). In the *pf33* axoneme, the spokehead and one of the two neck branches in RS1 are blurred (C), whereas the other branch (red arrow) is completely missing compared with the WT reference (A). The head and neck regions in RS2 (D) also appear blurry compared with the RS2 in WT (B). However, the upper branch in RS2 is more intense than that in RS1 (C). For best visualization of RSs, densities represent an average of 15 slices along the *z*-axis (corresponding to 8.4 nm, which covers the entire thickness of the bifurcated spokeneck as well as the spokestalk), and rotation along the *x*-axis by +20° angle with respect to Figure 2, A–C. Scale bar: 24 nm.

Heterogeneity of RSs in the *pf33* axoneme

To further analyze the structural defects in HSP40-minus RSs, we performed one-dimensional (1D) classification (Obbineni *et al.*, 2017) with aligned subvolumes (hereafter referred to as "particles"). The complete data set for the 96-nm periodicity-based average from *pf33* and the control full-length axonemes is presented in Figure 4. In the initial analysis, *pf33* particles can be categorized into two classes. Class A, composed of ~80% analyzed particles, has a flexure in one of the two branches at the bifurcated neck of RS1 (Figure 4A, red arrow) as well as overall weak RS head density (Figure 4A, red arrow) compared with the stalk. The remaining ~20% particles, class B, have a homogeneous density distribution along the spokes and represent a subpopulation of less-deformed spoke structures within the *pf33* mutant (Figure 4B). It is possible that the trace amount of HSP40 (Figure 1) contributes to normal morphological conformation of some RSs (Figure 4B).

Further classification of the particles within each class has shown an array of distortions in *pf33* RSs, especially those in class A (Figure 4, A1–3). Aside from the flexure of one of two branches in RS1's neck region (arrow in classes 4A and 4A3), A1 has a weaker density at the spokehead periphery compared with the rest of spokes, while A2 has a slight change in the orientation and overall flexibility at neck/head regions (Figure 4, A1 and A2, red arrows). As for class B, a 54% subpopulation (Figure 4B1) has a rather uniform density distribution along the spoke complex, similar to the 60% subpopulation of the class C control (Figure 4C and 4C1). The remaining subpopulations in both class B and in the control have subtle distortions in spokeneck and spokehead regions (Figure 4, B2, B3, and C2). Some of those might be attributed to experimental procedures (e.g., flattening during plunge-freezing procedure).

Synchronized assembly of HSP40 and flagella

Cofractionation of HSP40 with mature RSs but not RS precursors (Yang *et al.*, 2005) raises the question of how HSP40 becomes incorporated into RSs to confer structural homogeneity. We addressed this by monitoring the location of fluorescent HSP40 during the generation and repair of flagella in live cells. By PCR and cloning, we first recovered the entire HSP40 genomic DNA from WT cells and converted it into two plasmids, pHSP40 and pGFP (green fluorescent protein)-HSP40. Both constructs

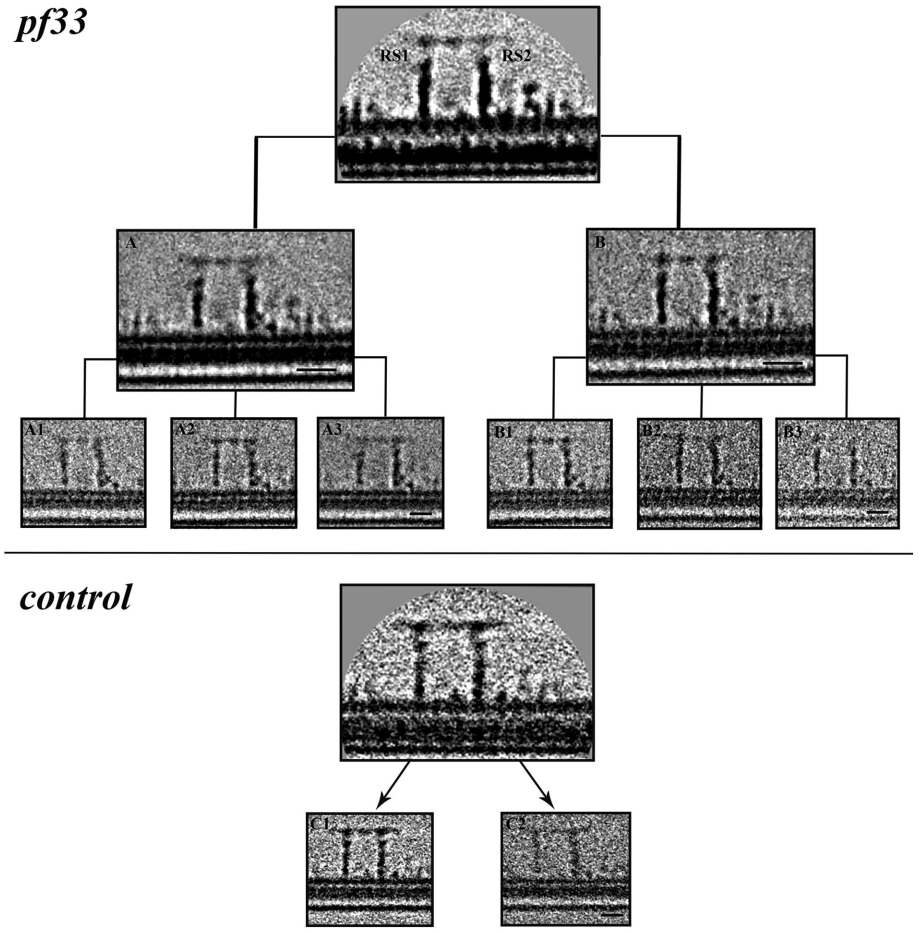

FIGURE 4: *pf33*: classification of RS complexes in *pf33* mutant axoneme. The 1D classification of subvolumes from the total average (*pf33*, top) results in two density maps (A, B). The subvolume representing class A, with ~80% of all particles ($N_A = 541$), has a distinct density at the interface between the spoke stalk and neck of RS1 (arrow in A). Particles in this class were further categorized into three subclasses, A1–A3 ($N_{A1} = 102$; $N_{A2} = 131$; $N_{A3} = 193$), each with a distinctive feature (red arrows). A1 has a weaker density at the spokehead periphery compared with the rest of the spokes. A2 has a slight change in the orientation of the RS2 neck region. A3, like class A, is prominent by the flexure of one branch in RS1 neck region (arrow in A3). The three subclasses from the particles forming class B ($N_B = 147$) have variations distinct from those of class A ($N_{B1} = 79$; $N_{B2} = 43$; $N_{B3} = 25$). B1 is very similar to class B, with homogeneous density distribution in the RS complexes. In contrast, B2 has a slight distortion at the neck of RS2. In B3, the density of the spokehead region (dashed rectangle) appears very weak, indicative of further heterogeneity in this region. Control: classification of RS complexes in the axoneme of a motile *pf14* transformant rescued by a full-length *RSP3* transgene. With applied classification procedures, the data set representing the total, 96 nm–based average has diverged into two distinct classes. The majority of particles (~60%) form class C1 ($N_{C1} = 269$) and have WT-like RS morphology with rather typical neck and head regions. The rest of particles are included in class C2 ($N_{C2} = 174$). The weak density of RS1 compared with RS2 suggests that RS1 might contain further structural variations that are not evident due to low signal-to-noise ratio of the particular class average. Scale bar: 24 nm.

restored normal motility to *pf33*. Western blots probed for HSP40 showed that GFP-HSP40 in the axoneme of motile *pf33* transformants was as abundant as HSP40 in the WT control (Figure 5A). This further confirms that the absence of HSP40 causes heterogeneous RS structures and jerky flagella in *pf33* and HSP40 RNAi strains. Live fluorescence microscopy showed that, contrary to the dark flagella of *pf33* cells (Figure 5B, left panel), entire flagella of rescued *pf33* transformants fluoresced evenly (right panel). Thus, HSP40 is distributed throughout flagella as RSs.

We then compared GFP-HSP40 assembly with flagellar regeneration. Following pH shock–triggered deflagellation of *pf33*::GFP-HSP40 cells, images were taken periodically within 1 h. Fluorescence appeared throughout nascent growing flagella visualized in bright-field microscopy (compare top and bottom panels in Figure 5C). Therefore, the assembly of GFP-HSP40, RSs, and flagella were synchronized.

Identical polarities but distinct efficiencies in the repair of HSP40 and RSs

Previous studies using dikaryon rescue (reviewed by Dutcher, 2014) showed that partial RS complexes were reparable. However, the process was not as defined as the restoration of intact RSs. Therefore, we tested whether *pf33*::GFP-HSP40 cells can donate GFP-HSP40 to repair HSP40-minus RSs in *pf33* flagella. *Chlamydomonas* gametes of opposite mating types fuse into a dikaryon with two nuclei and four flagella. During this stage, which lasts for ~2.5 h before flagella resorb, the cytosol contains components from both cells. This allows defects in one gamete to be complemented by normal proteins produced by its partner. It was demonstrated that RSs missing in *pf14* flagella due to the mutated *RSP3* gene were restored in dikaryons owing to RSP3 produced by *pf14*'s partner (Johnson and Rosenbaum, 1992). Notably, as revealed by RSP3 immunofluorescence, RS restoration initially appeared at the tip of paralyzed *pf14* flagella and then progressed toward the base (Figure 6, top panel). This result and other evidence support the model that prepackaged axonemal complexes, including RSs, are delivered by anterograde IFT to the flagellar tip to be assembled to the microtubule plus end for the growth of new flagella and the turnover of full-length flagella (Rosenbaum and Witman, 2002; Qin *et al.*, 2004). We reason that, if HSP40 is delivered by IFT as RS precursors, GFP-HSP40 will be also restored to the tip of *pf33* flagella first (bottom panel). However, if HSP40 diffuses into the axonemal lumen as small molecules like GFP (Luo *et al.*, 2017), then the fluorescence should appear at the base first. If the donor's HSP40 cannot enter flagella on its own, there will be no rescue.

To establish live imaging of RS dikaryon rescue, we mixed the gametes of *pf14*(–) and *pf14(+)::RSP3-GFP* cells. Afterward, the cell mixture was imaged about every 15 min with bright-field and fluorescence microscopy. Owing to time constraints and faint fluorescence, we only captured focused flagella in five or more dikaryons at each time point from two repeated experiments. As not all dikaryons form simultaneously, the dikaryon with the most extensive

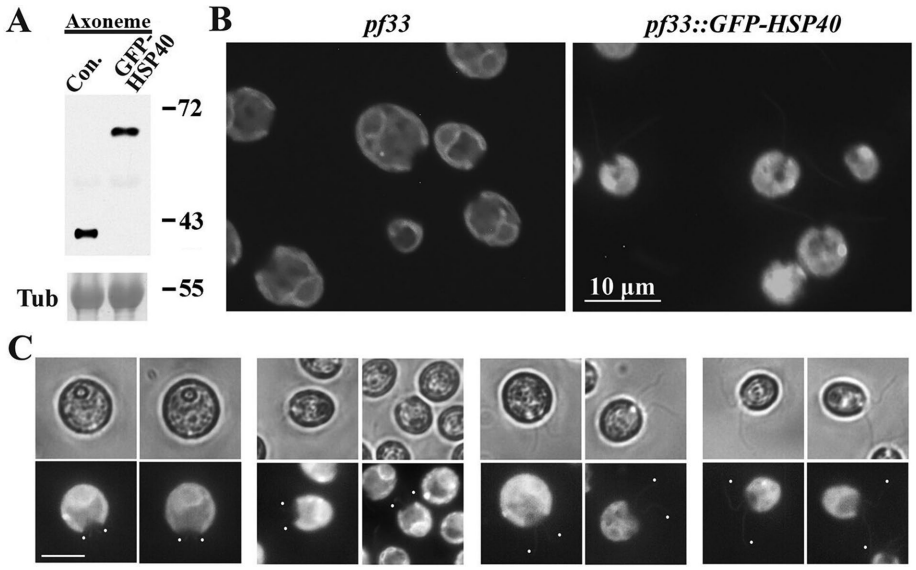

FIGURE 5: Synchronized assembly of HSP40 and RSs. (A) Western blot of axonemes probed with anti-HSP40 antibody shows similar abundance of HSP40 from WT control cells and GFP-HSP40 from motile *pf33* transformants. (B) Fluorescence microscopy of *pf33* and GFP-HSP40 transformants. With the focus on GFP-HSP40–illuminated flagella, fluorescence distributes uniformly throughout the length of flagella in all cells from a motile transformant strain. Intense background fluorescence in the cell body of both strains is primarily derived from plastids. (C) Fluorescence images of live *pf33::GFP-HSP40* cells taken periodically within 1 h following flagella excision. Fluorescence distributed throughout the regenerating flagella, regardless of the length. Dots show the tip of fluorescence. The experiment was performed three times. Cells from the same strain and same culture could vary in size. Scale bar: 10 µm.

signal in the receiver flagella is presented. Consistent with the previous study (Johnson and Rosenbaum, 1992), dikaryons were observed readily within 15 min after mixing, with faint fluorescence noticeable at the tip of flagella of receiver cells (Figure 7A, arrowheads). Fluorescence brightened and extended toward the base at subsequent time points. By 90 min, fluorescence was visible nearly throughout flagella. Thus RSP3-GFP could replicate RSP3 immunofluorescence of dikaryons.

As to the group of *pf33(+)×pf33(–)::GFP-HSP40*, dikaryons also formed within 15 min (Figure 7B, top panel), but GFP-HSP40 was still not detectable in receiver HSP40-minus flagella in any dikaryon at the 90-min time point (bottom panel). After 120 min, extensive searches in three experiments identified six dikaryons with GFP-HSP40 at the tip of receiver flagella (Figure 7B, bottom panel, arrowheads) before flagella resorbed. The tip-first recovery of GFP-HSP40 was identical to that of whole RSs, contrary to the base-first polarity predicted by the diffusion model. However, compared with the nearby flagella from donor cells (Figure 7B) and RSP3-GFP signal representing restored whole RSs at the 30-min time point (Figure 7A), the rescue of GFP-HSP40 was exceedingly slow and the signal was weak. The pseudocolored panel was used to make the signal evident.

To test whether the poor repair of missing HSP40 was due to low abundance of GFP-HSP40 or the lack of de novo RS assembly, we conducted experiments using *pf33* gametes that were regenerating flagella (Johnson and Rosenbaum, 1992). Flagella of *pf33* cells were first amputated by pH shock. When new flagella grew back to about half length or two-thirds in the presence of cycloheximide that inhibited protein synthesis, the suspension was mixed with *pf33(–)::GFP-HSP40* cells with full-length flagella. In theory, generation of the proximal part of new flagella would largely deplete existing axonemal components available in the *pf33* cytosol, while the distal part generated after fusion would mostly come from proteins produced by the donor cell, including GFP-HSP40. As cells with short flagella mated less efficiently, the cell mixture was imaged 60 min after mixing, allowing gametes with long and short flagella to find each other, and short flagella to finish regeneration. We successfully imaged six randomly selected dikaryons with donor and receiver flagella in focus. As expected, fluorescence distributed throughout two flagella of donor cells and only at the new, distal part of the flagella of receiver cells (Figure 7C, arrowheads). The fluorescence in receiver flagella varied in intensity—some were nearly as intense as the donor's flagella (Figure 7C, the top cells in the left panel), whereas some others were dimmer (right panel), perhaps due to partial inhibition of protein synthesis or partial depletion of axonemal components in the receiving cell. Nonetheless, the rescue of GFP-HSP40 with de novo RS assembly occurred earlier and was evident without (Figure 7C, middle panels) or with pseudocolor (bottom panels).

Fluorescence intensity at the brightest spot near the tips of adjacent receiver (R) and donor (D) flagella in dikaryons of the three experiments was quantified. The intensity ratio (R/D in Figure 7D) showed that restoration of GFP-HSP40 to full-length flagella with HSP40-minus RSs after 120 min (middle bar) was significantly lower than restoration of whole RS to existing flagella (left bar, $p < 0.001$) or de novo assembly of GFP-HSP40 with RSs in growing flagella (right bar, $p < 0.001$) measured at least 1 h earlier. Together, these data suggest that, although HSP40 and RS precursor appear as separate particles in in vitro fractionations (Yang *et al.*, 2005), their trafficking and assembly in flagella are coupled.

No evident affinity between HSP40 and NDK5

Comparisons of RS deficiencies among mutants suggest that RSP2, NDK5, and HSP40 are located at the spoke neck of mature RSs (Table 1) (Huang *et al.*, 1981; Patel-King *et al.*, 2004; Yang *et al.*, 2005; Pigino *et al.*, 2011). While RSP2 is crucial for the assembly of all head and neck proteins, only NDK5 is directly required for the assembly of HSP40 (Zhu *et al.*, 2017b). To test whether HSP40 and NDK5 interact directly, we performed a pull-down assay, which was used to identify interacting RSPs (Kohno *et al.*, 2011). We first characterized individual polypeptides suitable for in vitro studies. While full-length recombinant NDK5 precipitated, the conserved N-terminal 201 amino acids (a.a.), including the NDK domain and the Dpy30 domain, were soluble and exhibited NDK activity (Zhu *et al.*, 2017b). Therefore, we hypothesize that algal NDK5's calmodulin-binding C-terminal tail of nearly 400 a.a. (Patel-King *et al.*, 2004) is dispensable for HSP40 assembly. Indeed, *ndk5* mutant cells become motile, with fluorescence distributed evenly along flagella (Figure 8A), when transformed with the plasmid pNDK5ΔC-Neongreen (NG), similar to the strains transformed with the plasmid expressing intact NDK5-NG (Zhu *et al.*, 2017b). NDK5ΔC-NG contains the first 201 a.a. and a short linker sequence and NG that is 2.7-fold brighter than enhanced GFP (EGFP). Interestingly, only the cells producing NDK5ΔC-NG cannot steer properly under

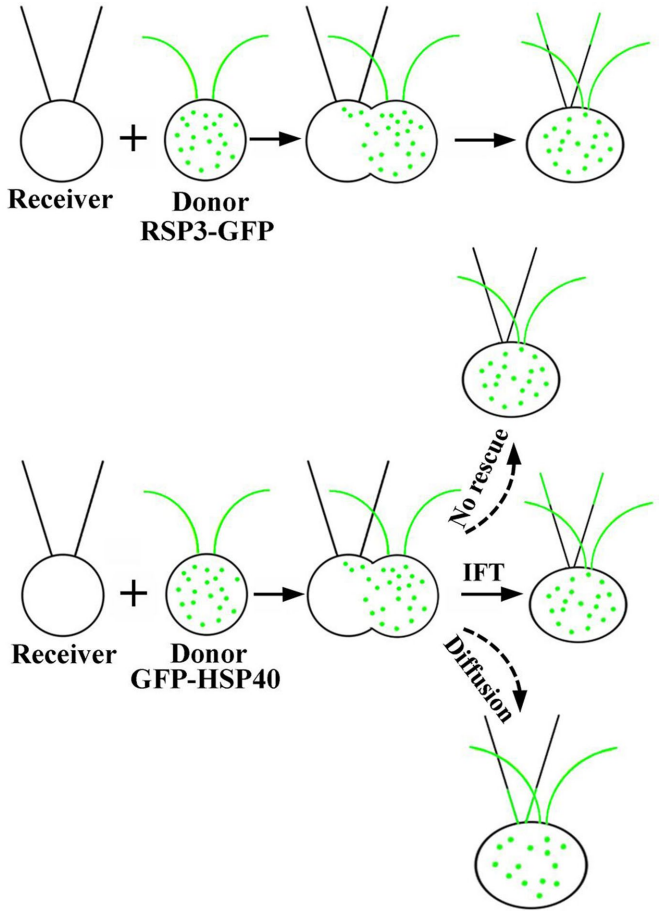

FIGURE 6: Possible outcomes of dikaryon rescue experiments testing how HSP40 is transported and assembled. Immunofluorescence shows that RSs are restored to the RS-free flagella in the RSP3 mutant *pf14* when a *pf14* cell is fused to a WT donor cell. The same results are expected in the control group using motile *pf14::RSP-GFP* as donor cells. Illustrated are three possible outcomes for dikaryons of *pf33* by the donor cell, *pf33::GFP-HSP40*. If HSP40 is delivered by IFT as RSs, the rescue pattern will be similar to the repair of *pf14* flagella. If HSP40 cannot enter flagella, there will be no repair. On the other hand, if HSP40 diffuses into flagella, perhaps through the axonemal lumen, the fluorescence will appear in a base-to-tip direction.

bright illumination, resembling RSP2ΔC transgenic cells that also lack a diverged calmodulin-binding C-terminal tail (Gopal *et al.*, 2012). Thus, the conserved $NDK5_{1–201}$ is sufficient for HSP40 assembly and rhythmic beating, while the diverged C-terminus is required for light-related steering of photosynthetic green algae.

Recombinant HSP40 can rescue the motility of HSP40-minus RNAi cells upon electroporation (Yang *et al.*, 2008). To test the oligomeric state, we performed analytical ultracentrifugation velocity sedimentation experiments. In the 5- to 50-μM concentration range, the c(S) distribution showed a single peak, with an s_w value of 5 S. This corresponds to a molecular mass of 81 kDa (Figure 8B) and is consistent with dimeric HSP40 (theoretical molecular weight of monomer is 39 kDa). The formation of HSP40 dimers in solution is in a good agreement with the previous estimation of two HSP40 molecules in the neck region (Pigino *et al.*, 2011) and with canonical HSP40s (Kampinga and Craig, 2010).

For the pull-down assay, we mixed together affinity-purified His-tagged HSP40 and His-tobacco etch virus protease (TEV)-$NDK5_{1–201}$ expressed separately in bacteria. His-tagged TEV protease was added to the mixture to cut off the His tag from $NDK5_{1–201}$. After overnight incubation, the mixture was subjected to the second round of affinity purification. Coomassie blue–stained gel showed that most His-TEV-NDK5 lost the tag (Figure 8C, compare the first lane in the left and middle panels), resulting in fast-migrating untagged NDK5 in the flowthrough (Post in the middle panel), while His-TEV and residual His-NDK5 were present in the eluate, pulled down by nickel-nitrilotriacetic acid (Ni-NTA). Interestingly, the untagged NDK5 was in the flowthrough (Post in the right panel), separated from His-HSP40 in the eluate. Therefore, although the conserved NDK5 region is directly required for HSP40 assembly in vivo (Zhu *et al.*, 2017b), and both recombinant proteins appear active in vitro and in vivo, they exhibit no evident affinity to each other. Thus, it is unlikely that HSP40 simply binds to NDK5 to adhere constitutively to RSs.

DISCUSSION

Despite considerable investigations of chaperones, much about the extensive repertoire of HSP40 isoforms remains to be elucidated. By taking advantage of the well-defined RS complex and the available tools for *Chlamydomonas*, this study has shed new light on HSP40s and flagellar biology.

HSP40 stabilizes the spokehead complex to facilitate RS–CP interactions

An absence of HSP40, but not the nearby RSP2 and NDK5, does not lead to missing RS structures or components (Pigino *et al.*, 2011; Zhu *et al.*, 2017b). Our sub-tomogram averaging of the HSP40 mutant axoneme, together with a 1D classification analysis, reveals the structural impact of HSP40 in the spoke complex in situ. The weak densities in the spokehead and spokeneck regions (Figures 2 and 3) suggest structural flexibility. This is consistent with the various deformed RSs of low resolution in thin-section images (Figure 1B; Yang *et al.*, 2008) and explains the jerky, rather than paralyzed, motility phenotype of the *pf33* axoneme. High flexibility in the spokeneck and spokehead could probably hinder proper spokehead interactions with the CP complex and subsequent mechanical transduction through the stalk to outer doublets. Thus, for the rhythmic beating of flagella, it is crucial that all components in the RS head–neck region not only are present but also assemble into a certain stable conformation, relative to the CP complex, that permits their intermittent contacts, in synchrony with flagellar beating. These results support the importance of the direct RS–CP contact (Oda *et al.*, 2014) and the model of rather specific RS–CP interactions with a preferential binding to corresponding CP projections in vivo (Nakazawa *et al.*, 2014).

Interestingly, absence of HSP40 results in distinct types of defects in RS1 and RS2, which appear more prominent in RS1 (Figure 4). While a subpopulation of RS1 has a distortion in one of the bifurcated neck branches, RS2's changes are primarily limited to its orientation. Thus, in the absence of HSP40, the mature Y-shaped spoke complex could be assembled, albeit in a rather flexible state. Notably, RS1 is anchored near the two-headed inner dynein arm, a major target of phosphoregulation, whereas RS2 is anchored near single-headed dynein arms (reviewed by Zhu *et al.*, 2017a). Thus, RS1 and RS2 may encounter distinct forces from their respective microenvironments in beating flagella, leading to their distinct deformation propensity when HSP40 is absent. On the basis of these observations, we propose that HSP40 locks the mature RS into a conformation of heightened rigidity to facilitate intermittent spokehead–CP interactions that permit rhythmic flagellar beating.

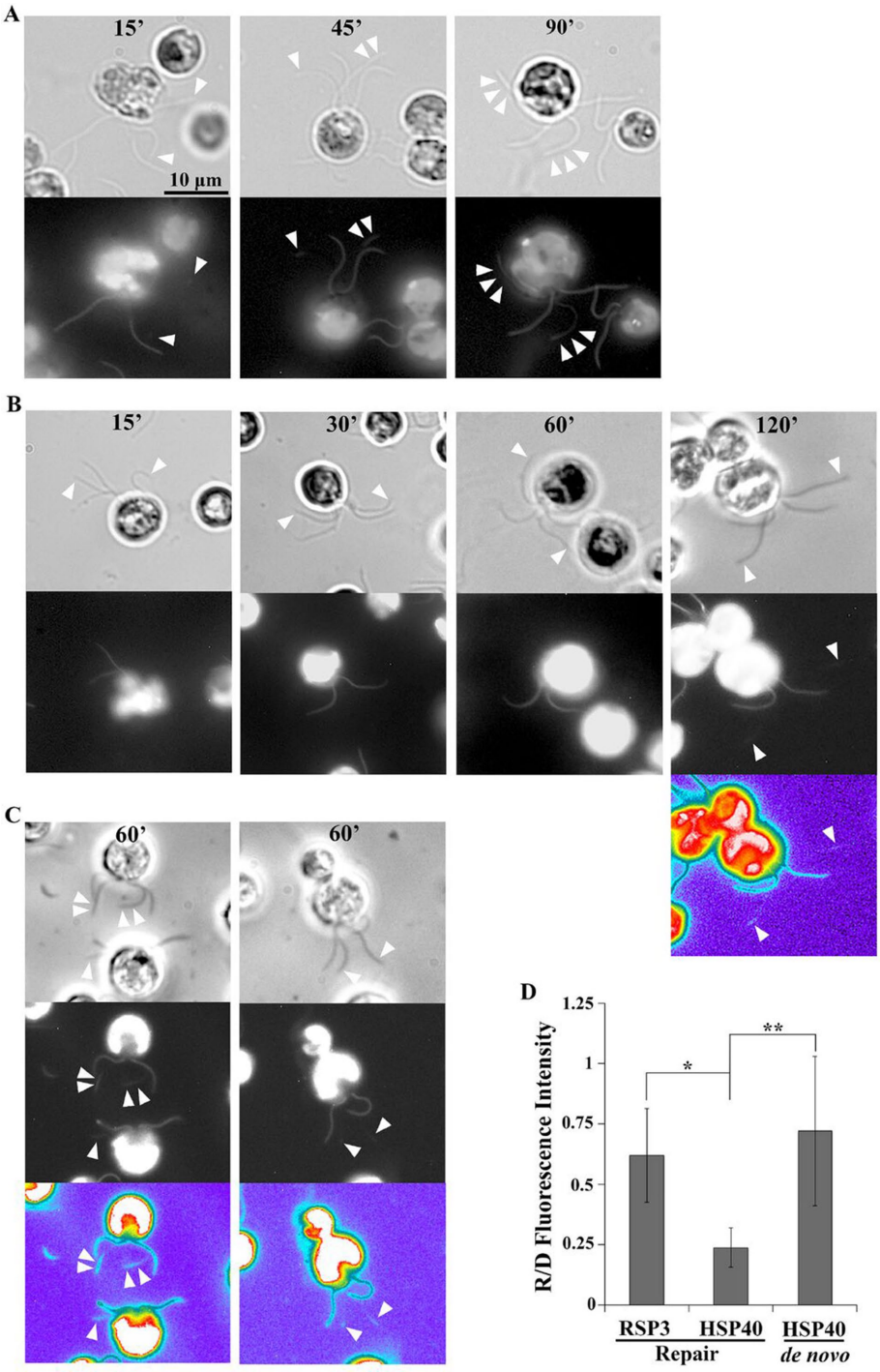

FIGURE 7: Distinct efficiencies in the repair of missing RSs and HSP40 in dikaryon rescues. Cells were imaged by bright-field (top) and fluorescence (bottom) microscopy approximately every 15 min after cells of opposite mating types were mixed. Each image represents at least five dikaryons. (A) Dikaryons of *pf14*(–) by *pf14(+)::RSP3-GFP*. Fluorescence, already detectable at the tips of receiver *pf14(+)* flagella after 15 min (arrowheads), extended toward the base and became stronger as time progressed. The experiment was performed twice. (B) Delayed restoration of GFP-HSP40 to receiver *pf33(+)* flagella from *pf33(–)::GFP-HSP40*. Fluorescence was not detectable in receiver *pf33* flagella until 120 min after mixing. Fluorescence also appeared at the flagellar tip (arrowheads) of six dikaryons among many observed at the 120-min time point from a total of three experiments, but the intensity was exceedingly dim. Pseudocolor was used to highlight the restoration. Flagella were shed soon afterward. The experiment was performed three times. (C) Efficient restoration of GFP-HSP40 along with de novo assembly of RSs in newly generated flagella of dikaryons. At 30 min after flagellar excision, *pf33(+)* with half-length regenerating flagella was mixed with *pf33(–)::GFP-HSP40* with full-length flagella. GFP-HSP40 was restored to the distal part of growing HSP40-minus flagella of *pf33(+)* in all dikaryons at 60 min after mixing. Fluorescence intensity in regenerating receiver flagella varies. All dikaryon rescue experiments were performed in the presence of cycloheximide to inhibit protein synthesis. The experiment was performed once. (D) Comparison of fluorescence intensity in dikaryons' flagella. Fluorescence intensity at the brightest region near the flagellar tip was measured. Averaged receiver vs. donor (R/D) intensity ratio and SD at the flagellar tip was 0.62 ± 0.19 (n = 13, from 15- to 60-min time points) for restored RSs with RSP3-GFP, 0.24 ± 0.08 (n = 8, from 120-min time points) for GFP-HSP40 restored to existing RSs, and 0.72 ± 0.3 (n = 9, from 60-min time points) for de novo assembly of GFP-HSP40 and flagellar assembly. Only flagella from the same dikaryons and in focus were used for comparison. HSP40 repair is significantly lower than RS/RSP3 repair (*, Student's t test, $p < 0.001$) and lower than the de novo assembly of GFP-HSP40 into RSs in growing flagella (**, Student's t test, $p < 0.001$). Asterisks indicate statistically significant differences.

Implications of the delayed tip-to-base repair of HSP40-minus RSs

Real-time imaging of dikaryon experiments (Figure 7) offers alternatives to the interpretation based on separate HSP40 and RS precursor particles in both velocity sedimentation and chromatography (Yang *et al.*, 2005). The identical polarity for the restoration of HSP40 and RSs in dikaryons (Figure 7, A and B) strongly suggests that HSP40, like RS precursors, also has to reach the tip first to be restored to the receiver flagella. However, the slow, limited repair, even after 2 h, is contrary to evident repair of whole RSs (Figure 7A) and other axonemal complexes (e.g., Piperno *et al.*, 1996) within 30 min and to the synchronized de novo assembly of GFP-HSP40 along with RSs in regenerating flagella in typical cells or dikaryons (Figures 5C and 7C). This cannot be explained by diffusion of free HSP40, which is inconsistent with the tip-to-base restoration of GFP-HSP40 (Figure 7B). Furthermore, diffusion of small molecules in flagella is not slower than IFT (Ye *et al.*, 2013; Harris *et al.*, 2016). Nor can it be attributed to poor accessibility of RSs located within the ring of outer doublets to HSP40 located outside the ring, because electroporation of recombinant HSP40 rescued the motility of HSP40-minus cells almost immediately (Yang *et al.*, 2008). Thus, the simplest explanation is that HSP40 and RSs are coupled in trafficking and assembly. If HSP40 binds to RS precursors on the way

	Strain	Causative gene	Deficient subunits	References
Head mutants	*pf1*	*RSP4*	RSP1, 4, 6, 9, and 10	McVittie, 1972 Huang *et al.*, 1981 Curry *et al.*, 1992
	pf26	*RSP6*	RSP1, 4, 6, 9, and 10	Curry *et al.*, 1992 Wei *et al.*, 2010
	pf17	*RSP9*	RSP1, 4, 6, 9, and 10	Huang *et al.*, 1981
Neck mutants	*pf24*	*RSP2*	RSP1, 4, 6, 9, and 10; RSP2; NDK5; HSP40	Huang *et al.*, 1981 Patel-King *et al.*, 2004 Yang *et al.*, 2004
	ndk5	*NDK5*	RSP1; NDK5; HSP40	Zhu *et al.*, 2017b
	pf33	*HSP40*	HSP40	Yang *et al.*, 2005, 2008

TABLE 1: *Chlamydomonas* mutant strains deficient in the head or neck region of the radial spoke.

to the tip like most RSPs, in dikaryons GFP-HSP40 molecules could only become integrated into the HSP40-minus axoneme after they dissociate from their trafficking partner or by de novo RS assembly when outer doublets turn over (Marshall and Rosenbaum, 2001). Consequently, the repair of HSP40 is slow. If so, separate HSP40 and RS precursor particles observed in biochemical fractionations (Yang *et al.*, 2005) may be caused by the disruption of typically transient cargo–chaperone interactions. We cannot rule out the possibility that IFT delivers HSP40 and RSs independently, but the GFP tag may hinder its delivery or its repair of preexisting HSP40-minus RSs. In this case, HSP40 should be somehow tethered to IFT trains.

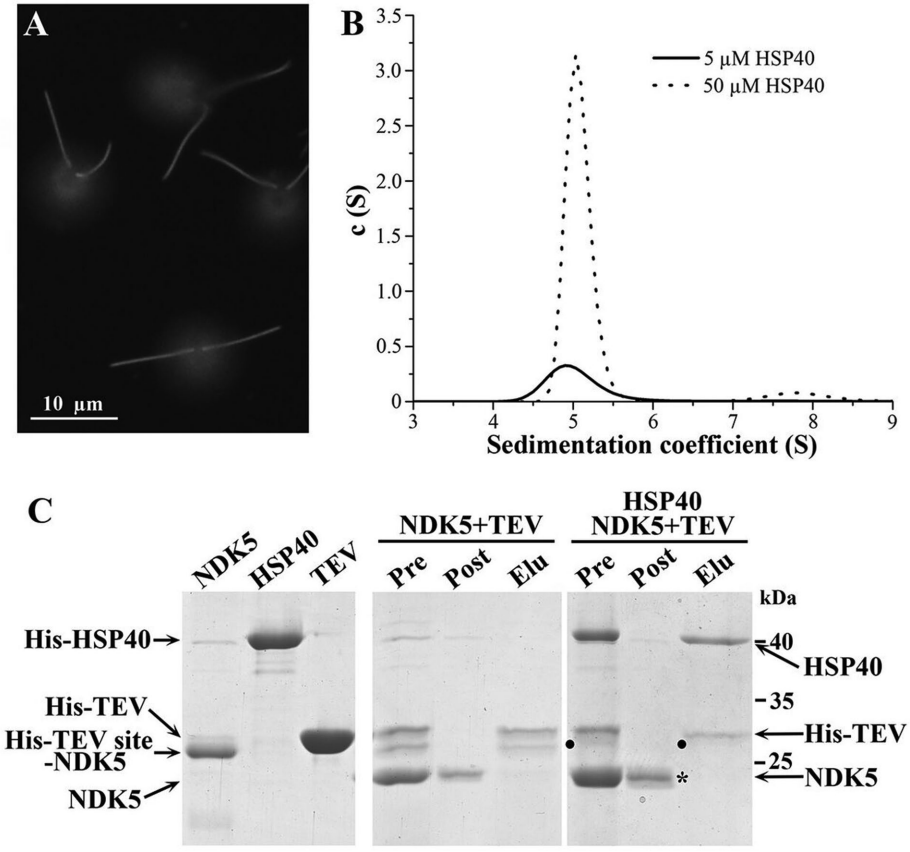

FIGURE 8: Analysis of the interaction of HSP40 and NDK5. (A) Live fluorescence imaging of *ndk5* transformant expressing NDK5ΔC-Neongreen. The fragment containing the conserved 1–201 a.a. rescued the *ndk5* mutant. Fluorescence distributed evenly throughout flagella as expected of RSs. Thus, this region is sufficient for the assembly of HSP40. Scale bar: 5 μm. (B) Analytical ultracentrifugation of recombinant HSP40. c(S) distribution of HSP40 shows a single peak with an s_w value of 5 S, which is consistent with a dimer formation. (C) Little copurification of His-HSP40 and $NDK5_{1–201}$ in vitro. His-tagged $NDK5_{1–201}$ (dot), HSP40, and TEV protease were expressed individually in bacteria and affinity purified with Ni-NTA (left panel). In the presence of His-TEV, His-$NDK5_{1–201}$ that had a TEV cleavage site was incubated overnight without or with HSP40. The mixture (Pre) was then subjected to Ni-NTA purification. Cleaved $NDK5_{1–201}$ (asterisk) was in the flowthrough (Post) regardless of the absence (middle panel) or presence (right panel) of His-HSP40 that, alone with His-TEV, was pulled down by Ni-NTA (in the eluate [Elu]). Samples were revealed by Coomassie blue–stained protein gels.

Slow repairs may not be unique to HSP40. In similar studies that use dikaryon rescue to reveal the genes causative to partial RS defects, repair signals were weak even though flagella were harvested 2.5 h after gamete mixing (Luck *et al.*, 1977; Huang *et al.*, 1981). Slow repairs of partial complexes are consistent with emerging evidence of IFT cargo adaptors for tubulins and likely respective axonemal complexes (Hou *et al.*, 2007, Hou and Witman, 2017; Ahmed *et al.*, 2008; Bhogaraju *et al.*, 2013). The specificity and mechanism of cargo–adaptor associations are still emerging (reviewed by Pedersen, 2016). In theory, with adaptors, IFT could deliver various intact complexes and tubulins in synchrony to the tip to grow new flagella or to restore missing complexes if flagella have formed (Figure 7, A and C; Johnson and Rosenbaum, 1992). In contrast, repairs of incomplete axonemal complexes in full-length flagella are expected to be inefficient, unless some adaptors have a broad specificity; non-IFT trafficking paradigms are involved in repairs; axonemal turnover could be accelerated; or precursors and defective complexes in axonemes can swap components. These new ideas can be tested by studying the repair of partial defects in other *Chlamydomonas* mutants (Piperno *et al.*, 1996; Lechtreck *et al.*, 2013; Dutcher, 2014). The findings will guide emerging gene therapy for primary cilia dyskinesia (McIntyre *et al.*, 2013) that could

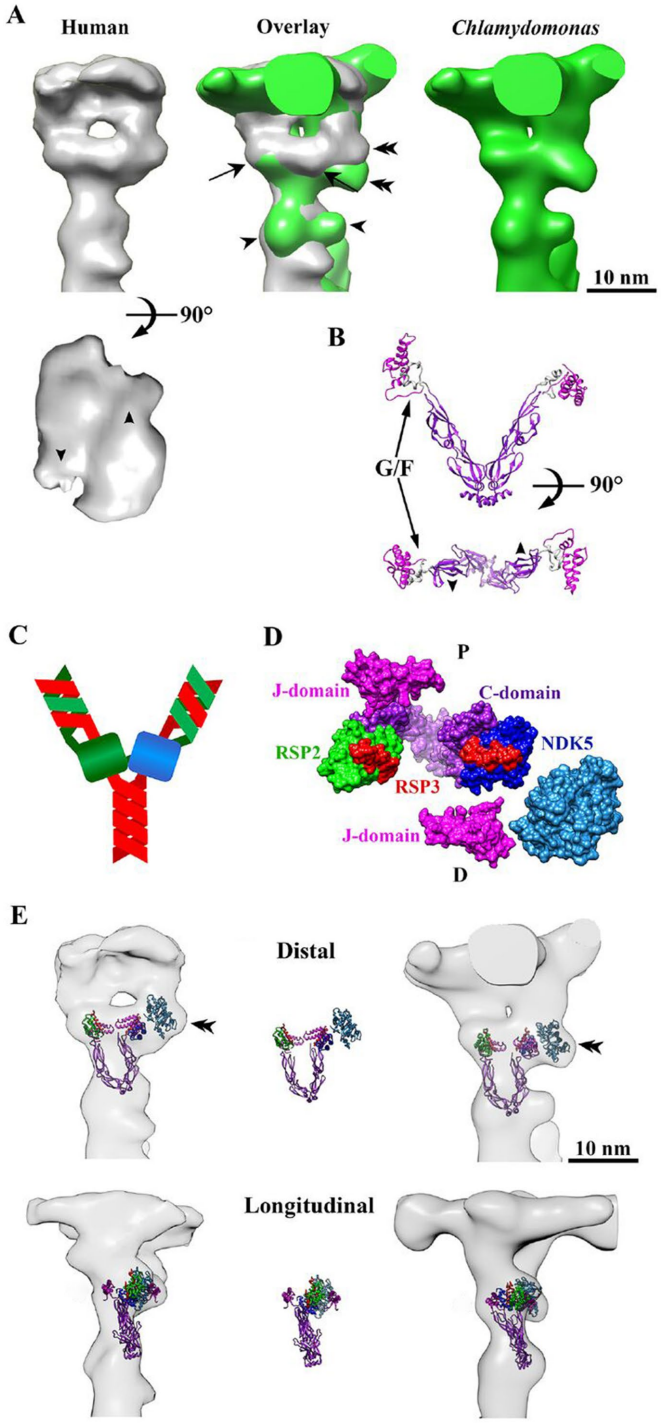

FIGURE 9: Structural modeling of the RS neck region. (A) The distal view of the second RS (RS2) in each axonemal repeat from human (left panel; Electron Microscopy Data Bank [EMDB] accession number: 5950; Lin *et al.*, 2014) and *Chlamydomonas* (right panel; EMDB accession number: 1941; Pigino *et al.*, 2011). The overlay (middle panel) highlights the bifurcated neck with a nodule (arrow) below each branch and an asymmetric protrusion (double arrowheads). The top view shows two head modules positioned in twofold rotational symmetry (arrowheads of opposite orientation in the bottom panel). (B) The crystal structure of a dimeric bacterial HSP40 (PDB accession number: 4J80), with the G/F region between J domains to the V-shaped C domain dimer. It also exhibits rotational symmetry when viewed after a 90° rotation. (C) Schematic depicting the proposed RS structure core composed of homodimers of RSP3 (red) and RSP2's (green) and NDK5's (blue) Dpy30 domains. (D) Top view of a space-filled model illustrating the predicted key structural components in the region below the bifurcated branches. P, proximal; D, distal. (E) Distal view (top panel) and longitudinal view (bottom panel) of ribbon models overlaying human RS2 (left panels) and *Chlamydomonas* RS2 (right panels). Each of the neck nodules (arrows) harbors a unit of an AH from RSP3 (red) that anchors a Dpy30 domain homodimer from RSP2 (green) or NDK5 (blue) (an equivalent structure from a Set1-like histone methyltransferase complex; PDB accession number: 4RIQ). The two units are clenched together by a J domain (magenta; PDB accession number: 2CTP) and the invisible flexible G/F-rich region that connects to the V-shaped C domain dimer (purple; PDB accession number: 3AGX). The NDK domain dimer of NDK5 (cyan, represented by NDK1; PDB accession number: 4ENO) is placed in the asymmetric protrusion (double arrowheads).

be caused by diverse axonemal defects, including those lacking a functional HSP40 (El Khouri *et al.*, 2016).

Structural modeling of HSP40 and the spokeneck

We placed relevant domains into RS surface renderings from cryo-electron tomograms with the Chimera program to envisage how HSP40 may stabilize the neck region. We evaluated only RS2 (Figure 9A), which is similar to RS1 at the neck (Lin *et al.*, 2014; Pigino *et al.*, 2011). This bifurcated region has two prominent nodules (arrows, middle panel), each extending upward into a branch, which in turn connects to a spokehead module (Barber *et al.*, 2012; Lin *et al.*, 2012; Heuser *et al.*, 2012). Both algal and human RSs are modeled, because while algal RS is well defined, human RS is suited for modeling, because its spokehead is smaller, lacking the elaborate processes that may partly correspond to the alga-unique, dispensable sequences in several RSPs to be modeled in this study, including NDK5, RSP2, and RSP3 (Gopal *et al.*, 2012; Sivadas *et al.*, 2012; Oda *et al.*, 2014; Zhu *et al.*, 2017b). From a top view, the two-module spokehead exhibits a two-fold rotational symmetry (arrowheads in bottom panel). Interestingly, so does the sole crystal structure of an intact HSP40 dimer (Barends *et al.*, 2013), as viewed from the J domains, which connect to the V-shaped C-termini via a disordered G/F-rich domain (Figure 9B, arrowhead), supporting our notion that HSP40 stabilizes the flexible bifurcated region (Figure 4).

Our previous study predicts that the RS core is an RSP3 dimer (red ribbons in Figure 9C) (Yang *et al.*, 2008; Sivadas *et al.*, 2012; Oda *et al.*, 2014). The bifurcated neck is primarily formed by an amphipathic helix (AH) in one RSP3 molecule anchoring RSP2's Dpy30 domain dimer (green), allowing the adjacent short helices to fold into two neck branches. The AH from the second RSP3 anchors NDK5's Dpy30 domain dimer (blue). On this basis, we first place the Dpy30/AH complex from the Set1-like histone methyltransferase complex (Protein Data Bank [PDB] accession number: 4RIQ; Tremblay *et al.*, 2014) into each neck nodule to represent the same complex composed of RSP3's AH (red) and the dimer of the Dpy30 domain from RSP2 (green) or NDK5 (blue) (Figure 9D, top view). To fill up the additional space (distal views and side views in Figure 9E), we add HSP40's J-domain (magenta; PDB accession number: 2CTP) from the most homologous HSP40 isoforms. The G/F rich region is not modeled, because its sequence is highly divergent, corresponding to the disordered flexible structure, which can change in the presence of clients (Yan and Craig, 1999; Perales-Calvo *et al.*, 2010). We envisage that each J domain and the hidden G/F domain may encircle a Dpy30/AH module, whereas the V-shaped C-terminal dimer is positioned

below the neck (purple; PDB accession number: 3AGZ; Suzuki *et al.*, 2010). Into the asymmetric protrusion adjacent to NDK5's Dpy30 domain (Figure 9E, double arrowheads), we place the NDK domain dimer (cyan; PDB accession number: 4ENO; Kim *et al.*, 2013). Consistent with this, *Tetrahymena* lacks this protrusion (Pigino *et al.*, 2011) as well as the NDK5 gene (Zhu *et al.*, 2017a). This steric arrangement largely fits the space in RSs from humans (Figure 9E, left panels) and *Chlamydomonas* (right panels), with the dimeric HSP40 resembling two malleable front claws of crabs, bracing together the two Dpy30/AH modules. Alternatively, HSP40 is positioned mostly above the Dpy30 domains, with the claws clenching together the two neck branches and head modules. In either position, the claw-like HSP40 dimer could prevent the bifurcated regions from flexure or rotation during the beat cycle. The exact position of HSP40 and whether it interacts with multiple RSPs could be differentiated by high-resolution structural studies of bona fide RSPs and purified RSs, revealing the angle of HSP40's V-shaped C-terminal dimer and localizing its N- and C-termini in the axoneme.

The actions of HSP40

This crab-claw model, based on HSP40's general conformation and the true relative size of HSP40, NDK5, and the RS, strongly suggests that dimeric HSP40 stabilizes the RS by interacting with a swath of surfaces contributed by multiple RSPs, not just NDK5. This is concordant with HSP40's multivalent interactions with client polypeptides and HSP70 (Ahmad *et al.*, 2011), deformed HSP40-minus RS structural variants (Figures 2–4), and lack of affinity for NDK5 (Figure 8), which is directly responsible for HSP40 assembly. This model also sheds light on the slower motility of HSP40-null cells rescued by electroporated HSP40 lacking the J domain than those rescued by intact HSP40 (Yang *et al.*, 2008). Perhaps RSs partially stabilized by truncated HSP40 cannot consistently transduce mechanical feedback, leading to occasional asynchronous beats, zigzag trajectory, and a slower velocity, as seen in a mutant with a partial spokehead (Wei *et al.*, 2010). This implies that the conserved spoke's HSP40 J domain has a structural role, rather than activatation of HSP70 ATPase activity. Thus, the HSP70-activating HPD tripeptide is not conserved.

Structural modeling and the headless-like RS of the *ndk5* mutant despite the presence of spokehead proteins (Zhu *et al.*, 2017b) inspire us to propose a second model to explain the slow tip-to-base repair of HSP40-less flagella (Figure 7). We envisage that the HSP40 dimer associates with the Γ-shaped precursor during anterograde IFT, like escorting a client complex (Figure 10I), which relies on RSP2 to tether other head and neck components by docking its Dpy30 domain dimer to the AH of one RSP3 molecule. Upon exiting IFT at the flagellar tip, the second RSP3's AH becomes available to anchor NDK5's Dpy30 domain, switching the Γ shape into the Y-shaped intermediate flexible state (panel II), which is subsequently stabilized by the HSP40 dimer poised nearby wrapping around the neck (panel III) or the head region with its flexible G/F region and J domain. This assembly process may reverse (gray arrows) as RSs disassemble, unfolding back to Γ-shaped precursors for recycling in the cell body (Qin *et al.*, 2004). This prediction is supported by direct interaction of human RSP2 and NDK5 shown in the yeast two-hybrid system (Rual *et al.*, 2005); a structural unit of two purified Dpy30 domain dimers (Wang *et al.*, 2009); and deficiencies of RS mutants (Table 1). Therefore, rather than binding to HSP40 solely and directly, NDK5 may be responsible for the formation of a flexible Y-shaped intermediate state, which then becomes stabilized by binding to HSP40.

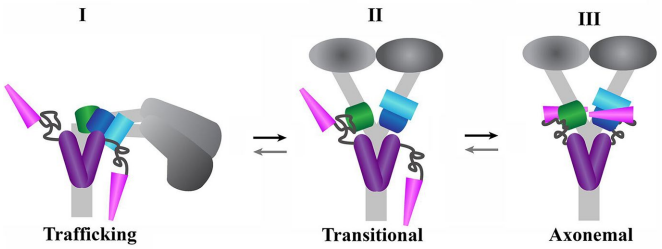

FIGURE 10: Schematic picture depicting coupled trafficking and refolding of HSP40 and its RS client. During trafficking, HSP40 dimer (magenta) tethers to the Γ-shaped RS precursor (panel I). RSP2's and NDK5's Dpy30 domains (green and blue) associate with each other but only RSP2's binds to RSP3's AH at the base of one arm. Upon their arrival at the flagellar tip, the precursor is released from IFT trains. With the AH in the second branch becoming available to anchor NDK5's Dpy30 domain dimer (blue), formalizing the Y-shaped, albeit flexible RS (panel II). This transformation induces the disordered G/F domains (wiggly lines) and J domains (pink) of HSP40 to refold around the Dpy30/AH module to stabilize mature RS (III). Refolding may occur near the spokehead if the V-shaped C-termini is positioned along the bifurcated branches. This process may reverse (gray arrows) when the RS is transported back to the cell body for recycling.

In summary, this study proposes that the cochaperone properties of HSP40s are harnessed for assembly processes that occur at two locations coupled by IFT. Without the involvement of HSP70, spoke HSP40 can operate very much like a chaperone—assisting the refolding of the spoke precursor into a mature configuration but staying afterward to maintain the structural rigidity and perhaps to allow unfolding of the mature complex back to the precursor for recycle. With remarkably malleable structures and partially diverged sequences, the numerous HSP40 isoforms may assist various polypeptides or molecular complexes in a similar manner—with or without HSP70s.

MATERIALS AND METHODS

Chlamydomonas reinhardtii strains, culture conditions, and biochemistry

The WT (cc124) and two *pf14* allelic mutants, cc613(–) and cc1032(+), were acquired from the *Chlamydomonas* Resource Center. The *pf33* mutant was generated by UV mutagenesis (Kamiya, 1988). The *pf14::RSP3-GFP* strain was generated by transformation of a RSP3 construct into the *pf14* allelic mutant (Zhu *et al.*, 2017b). Cells were grown in Tris-acetate-phosphate (TAP) media (Yang *et al.*, 2008). The light/dark cycle, flagella preparation, Western blot analysis, and antibodies were described previously (Yang *et al.*, 2001, 2006; Patel-King *et al.*, 2004).

Molecular biology

PCR-based genotyping. Approximately 1 µl of *pf33* and WT cells from TAP plates was resuspended in 40 µl of 10 mM EDTA. Following a 5-min boiling, 30-s vortex, and 3-min centrifugation, the supernatant containing genomic DNA was used immediately as template in PCR. The primer pairs were as follows:

P1S (GCAGTAAGTTACTTGGGTCTCAATGCG) and
P1As (GCAATTCAACTTACGATCGCAGAGC);
P2S (CGTGAGTTTGGGAGACTGTAGGGTCG) and
P2As (CGTGGAAGATCTCCTCCAGCGTAAGC);

P3S (GCTGTCCAACCAGTTCGAGTCCATGACC) and
P3As (CCTGTCCTCATGTAAACGCTCCAATCC);
P4S (GGTAACTTGGTCATTGAGATCGACCTGC) and
P4As (GCGGTAGTGCTCTTGGACATTTTGTGC).

Engineering of genomic constructs. The entire genomic *HSP40* gene was recovered by two rounds of PCR. In the first round, two primer pairs (GenS and P2As, P3S and GenAs) were used to amplify two overlapping genomic DNA fragments that include the 5′ and 3′ untranslated regions and the flanking sequences. The second round of PCR included equal amounts of the two fragments and the primer pair GenS and GenAs. The resulting full-length genomic DNA was inserted into pGEM-T Easy vector. A *Kpn*I-*Spe*I fragment purified from this plasmid was ligated into a plasmid containing the paromomycin (PMM)-resistant cassette (Sivadas *et al.*, 2012) for single plasmid transformation. The additional primers were

GenS (TGCCGTGTAAGGCCATGAGGCACACGC) and
GenAs (TCCCTTCTGCGCACCGTGTGCGGTACC).

For engineering the GFP-HSP40 genomic plasmid, GFP DNA (Rasala *et al.*, 2013) that was PCR-amplified using sense and antisense primers containing an *Nhe*I site (underlined) was cloned into the complementary *Xba*I site inserted downstream to the start codon of the HSP40 gene. The primers were

GFPS (GGCTAGCGATCCCCCCAAGGGCGAGG) and
GFPAs (GGCTAGCCTTGTACAGCTCGTCCATGCCGTGG).

The RSP3-GFP construct was derived by replacing the tag sequence in the RSP3-3HA12His construct (Gupta *et al.*, 2012) with the GFP DNA flanked by *Xho*I restriction sites.

Chlamydomonas experiments

Transformation. Genomic constructs were transformed into cells using a previously described glass bead method (Sivadas *et al.*, 2012). Transformants were selected on TAP plates containing 10 µg/ml PMM. A fraction of single colonies was resuspended in 200 µl of H_2O in 96-well plates for motility analysis under a Leica MZ16 stereo microscope.

Flagellar regeneration. Flagella of log-phase cells from TAP medium cultures were excised using pH shock. After microscopic confirmation of deflagellation, an aliquot of cells taken at the time indicated in Figure 7 was placed on polyethylenimine-coated slides for imaging.

Dikaryon rescue. A plate gametogenesis method (Martin and Goodenough, 1975) was used to produce gametes. Briefly, cells resuspended in H_2O were plated on TAP plates. After 5 d under constant light, cells were hatched first in H_2O and then supplemented with nitrogen-free TAP media. After being shaken under light for 4–5 h, equal amounts of gametes of opposite mating types were mixed and then placed under light without agitation. An aliquot of cells taken periodically as indicated was placed on polyethylenimine-coated slides for imaging. For creating dikaryons with two growing flagella and two full-length flagella, the experiment was performed as previously described (Johnson and Rosenbaum, 1992) with minor modifications. Briefly, recipient cells were triggered to shed flagella by pH shock. After confirmation of deflagellation microscopically, cells resuspended in 10 µg/ml cycloheximide in TAP media were allowed to regrow flagella to about half or two-thirds lengths and then mixed with donor cells of equal volume.

Flagellar isolation for cryo-ET. Axonemes were prepared from *full-length* rescued mutant and *pf33* strains of *C. reinhardtii* as previously described (Maheshwari *et al.*, 2015). In brief, flagella were isolated from the cells using dibucaine treatment. Membrane-free flagella or axonemes were spun down and used for cryo-ET.

Biochemical analysis

HSP40 purification. Recombinant HSP40 was produced by *Escherichia coli* carrying the coding sequence in the pProEx plasmid. Expression was induced by 1 mM isopropyl-β-D-thiogalactopyranosid for 12 h at 20°C. Cells suspended with 500 mM NaCl, 10 mM imidazole, 5 mM β-mercapthoethanol, and protease inhibitor cocktail (cOmplete, EDTA-free, Roche) in 50 mM HEPES (pH 7.5) were lysed by sonication. Following centrifugation at 30,000 rpm with a Ti45 rotor (Beckman Coulter, Indianapolis, IN) for 30 min at 4°C, His-HSP40 in supernatant filtered through 0.45-µm filter membranes was purified by the IMAC Ni^{2+} affinity chromatography with the AKTA express system following the instructions of the manufacturer (GE Healthcare Life Science, Wauwatosa, WI). The eluate was concentrated.

Analytical ultracentrifugation. Sedimentation velocity experiments were performed at 20°C and 42,000 rpm in a Beckman Coulter ProteomeLab XL-I analytical ultracentrifuge as described previously (Rezabkova *et al.*, 2016). Briefly, 400-µl aliquots of protein at different concentrations in 150 mM NaCl, 2 mM β-mercapthoethanol, 20 mM, and pH 7.5 HEPES were loaded into 12-mm charcoal-filled Epon double-sector center pieces. Data were analyzed in terms of a continuous c(S) distribution of Lamm equation solutions with the software SEDFIT (Schuck, 2003).

Pull-down assay. Expression of His-HSP40 and His-TEV-$NDK5_{1–201}$ and subsequent purification were described previously (Yang *et al.*, 2005; Zhu *et al.*, 2017b). His-TEV-$NDK5_{1–201}$ was treated with purified His-TEV protease overnight at 4°C in the presence or absence of His-HSP40 before Ni-NTA affinity purification.

Microscopy

Bright-field and fluorescence images were acquired at a 400× magnification using a Nikon Eclipse E600W compound microscope equipped with a CoolSNAP-ES CCD camera (Photometrics, Tucson, AZ) and MetaMorph imaging system (Molecular Devices, Sunnyvale, CA). The MetaMorph program was also used for pseudocolor with a standard rainbow color palette. ImageJ 1.50i was used to subtract background, and the line tool was used to draw across the brightest region near the flagellar tip to obtain plot profiles. The peak value from each profile was used to calculate intensity ratios. Thin-section EM of axonemes was performed as previously described (Kamiya, 1988).

Cryo-ET. Isolated axonemes were quickly frozen in liquid ethane at liquid nitrogen temperature with the help of a vitrification device (Cryo-plunge 3; Gatan, Pleasanton, CA). Holey carbon grids (200 mesh, R3.5/1; Quantifoil Micro Tools GmbH, Großlöbichau, Germany) were used. Gold colloid particles (10 nm) were applied to the sample before freezing as fiducial markers for tomographic reconstruction. Data collection was performed using a JEM2200FS transmission electron microscope (JEOL, Tokyo, Japan) equipped with an in-column energy filter and a field emission gun. Micrographs were recorded with a 4k × 4k CMOS camera (F416 from TVIPS, Gauting, Germany).

Sub-tomogram averaging and 1D classification. Tomographic image series were collected using a previously described procedure (Pigino *et al.*, 2011), except for the use of SerialEM software (Mastronarde, 2005). Image analysis was performed as described previously (Pigino *et al.*, 2011; Bui and Ishikawa, 2013). The final average of WT, *pf33*, and *pf24* axoneme was derived from, in total, 1332, 688, and 467 subvolumes, respectively, that were picked from reconstructed tomograms and aligned based on 24- and 96-nm periodic units. The final average of *full-length* rescued mutant (Sivadas *et al.*, 2012) contained 443 particles. The 1D classification was performed using a previously described procedure (Obbineni *et al.*, 2017). The mask used for classification included both RS1 and RS2 and was prepared with a 2-pixel smoothing.

Resolution estimation. Fourier shell correlation was measured using even/odd independent copies of masked volume using the EMBL-EBI online validation tool, whereby three different criteria are used for the proper evaluation of resolution (1/2 bit, σ-value, 0.5 and 0.143). Estimated resolutions were 3.9 nm for WT RS in Figure 2A (Pigino *et al.*, 2011) and 4.5 nm for *pf24* mutant strain.

Modeling

Crystal structures retrieved from the PDB were manually fitted into the surface renderings taken from the EMDB using Chimera UCSF (Pettersen *et al.*, 2004).

ACKNOWLEDGMENTS

We thank the Electron Microscopy Facility at the Paul Scherrer Institute (Switzerland) for technical assistance in EM data collection; and the lab of M. St. Maurice (Marquette University) for providing His-tag TEV protease. This work is supported by a Marquette University Startup and the National Institutes of Health (1R15GM128130-01) for P.Y. and a Swiss National Science Foundation grant (NF31003A 144035/1) for T.I. and E.P. X.Z. is supported by Marquette University fellowships. We thank J. M. Obbineni for his help with 1D classification analysis.

REFERENCES

Ahmad A, Bhattacharya A, McDonald RA, Cordes M, Ellington B, Bertelsen EB, Zuiderweg ER (2011). Heat shock protein 70 kDa chaperone/DnaJ cochaperone complex employs an unusual dynamic interface. Proc Natl Acad Sci USA 108, 18966–18971.

Ahmed NT, Gao C, Lucker BF, Cole DG, Mitchell DR (2008). ODA16 aids axonemal outer row dynein assembly through an interaction with the intraflagellar transport machinery. J Cell Biol 183, 313–322.

Ajit Tamadaddi C, Sahi C (2016). J domain independent functions of J proteins. Cell Stress Chaperones 21, 563–570.

Barber CF, Heuser T, Carbajal-Gonzalez BI, Botchkarev VV Jr, Nicastro D (2012). Three-dimensional structure of the radial spokes reveals heterogeneity and interactions with dyneins in *Chlamydomonas* flagella. Mol Biol Cell 23, 111–120.

Barends TR, Brosi RW, Steinmetz A, Scherer A, Hartmann E, Eschenbach J, Lorenz T, Seidel R, Shoeman RL, Zimmermann S, *et al.* (2013). Combining crystallography and EPR: crystal and solution structures of the multidomain cochaperone DnaJ. Acta Crystallogr D Biol Crystallogr 69, 1540–1552.

Bhogaraju S, Cajanek L, Fort C, Blisnick T, Weber K, Taschner M, Mizuno N, Lamla S, Bastin P, Nigg EA, Lorentzen E (2013). Molecular basis of tubulin transport within the cilium by IFT74 and IFT81. Science 341, 1009–1012.

Bloch MA, Johnson KA (1995). Identification of a molecular chaperone in the eukaryotic flagellum and its localization to the site of microtubule assembly. J Cell Sci 108 (Pt 11), 3541–3545.

Bui KH, Ishikawa T (2013). 3D structural analysis of flagella/cilia by cryo-electron tomography. Cilia Pt A 524, 305–323.

Bui KH, Yagi I, Yamamoto R, Kamiya R, Ishikawa I (2012). Polarity and asymmetry in the arrangement of dynein and related structures in the Chlamydomonas axoneme. J Cell Biol 198, 913–925.

Curry AM, Williams BD, Rosenbaum JL (1992). Sequence analysis reveals homology between two proteins of the flagellar radial spoke. Mol Cell Biol 12, 3967–3977.

Diener DR, Yang P, Geimer S, Cole DG, Sale WS, Rosenbaum JL (2011). Sequential assembly of flagellar radial spokes. Cytoskeleton (Hoboken) 68, 389–400.

Dutcher SK (2014). The awesome power of dikaryons for studying flagella and basal bodies in *Chlamydomonas reinhardtii*. Cytoskeleton (Hoboken) 71, 79–94.

El Khouri E, Thomas L, Jeanson L, Bequignon E, Vallette B, Duquesnoy P, Montantin G, Copin B, Dastot-Le Moal F, Blanchon S, *et al.* (2016). Mutations in DNAJB13, encoding an HSP40 family member, cause primary ciliary dyskinesia and male infertility. Am J Hum Genet 99, 489–500.

Fowkes ME, Mitchell DR (1998). The role of preassembled cytoplasmic complexes in assembly of flagellar dynein subunits. Mol Biol Cell 9, 2337–2347.

Gallaher SD, Fitz-Gibbon ST, Glaesener AG, Pellegrini M, Merchant SS (2015). *Chlamydomonas* genome resource for laboratory strains reveals a mosaic of sequence variation, identifies true strain histories, and enables strain-specific studies. Plant Cell 27, 2335–2352.

Gopal R, Foster KW, Yang P (2012). The DPY-30 domain and its flanking sequence mediate the assembly and modulation of flagellar radial spoke complexes. Mol Cell Biol 32, 4012–4024.

Gupta A, Diener DR, Sivadas P, Rosenbaum JL, Yang P (2012). The versatile molecular complex component LC8 promotes several distinct steps of flagellar assembly. J Cell Biol 198, 115–126.

Hageman J, Rujano MA, van Waarde MA, Kakkar V, Dirks RP, Govorukhina N, Oosterveld-Hut HM, Lubsen NH, Kampinga HH (2010). A DNAJB chaperone subfamily with HDAC-dependent activities suppresses toxic protein aggregation. Mol Cell 37, 355–369.

Harris JA, Liu Y, Yang P, Kner P, Lechtreck KF (2016). Single-particle imaging reveals intraflagellar transport-independent transport and accumulation of EB1 in *Chlamydomonas* flagella. Mol Biol Cell 27, 295–307.

Heuser T, Dymek EE, Lin J, Smith EF, Nicastro D (2012). The CSC connects three major axonemal complexes involved in dynein regulation. Mol Biol Cell 23, 3143–3155.

Hou Y, Qin H, Follit JA, Pazour GJ, Rosenbaum JL, Witman GB (2007). Functional analysis of an individual IFT protein: IFT46 is required for transport of outer dynein arms into flagella. J Cell Biol 176, 653–665.

Hou Y, Witman GB (2017). The N-terminus of IFT46 mediates intraflagellar transport of outer arm dynein and its cargo-adaptor ODA16. Mol Biol Cell 28, 2420–2433.

Huang B, Piperno G, Ramanis Z, Luck DJ (1981). Radial spokes of *Chlamydomonas* flagella: genetic analysis of assembly and function. J Cell Biol 88, 80–88.

Ito N, Kamiguchi K, Nakanishi K, Sokolovskya A, Hirohashi Y, Tamura Y, Murai A, Yamamoto E, Kanaseki T, Tsukahara T, *et al.* (2016). A novel nuclear DnaJ protein, DNAJC8, can suppress the formation of spinocerebellar ataxia 3 polyglutamine aggregation in a J-domain independent manner. Biochem Biophys Res Commun 474, 626–633.

Johnson KA, Rosenbaum JL (1992). Polarity of flagellar assembly in *Chlamydomonas*. J Cell Biol 119, 1605–1611.

Kamiya R (1988). Mutations at twelve independent loci result in absence of outer dynein arms in *Chlamydomonas reinhardtii*. J Cell Biol 107, 2253–2258.

Kampinga HH, Craig EA (2010). The HSP70 chaperone machinery: J proteins as drivers of functional specificity. Nat Rev Mol Cell Biol 11, 579–592.

Kim KS, Kustu S, Inwood W (2006). Natural history of transposition in the green alga *Chlamydomonas reinhardtii*: use of the AMT4 locus as an experimental system. Genetics 173, 2005–2019.

Kim MS, Jeong J, Jeong J, Shin DH, Lee KJ (2013). Structure of Nm23-H1 under oxidative conditions. Acta Crystallogr D Biol Crystallogr 69, 669–680.

Kohno T, Wakabayashi K, Diener DR, Rosenbaum JL, Kamiya R (2011). Subunit interactions within the *Chlamydomonas* flagellar spokehead. Cytoskeleton (Hoboken) 68, 237–246.

Lechtreck KF, Gould TJ, Witman GB (2013). Flagellar central pair assembly in *Chlamydomonas reinhardtii*. Cilia 2, 15.

Lechtreck KF, Mengoni I, Okivie B, Hilderhoff KB (2018). In vivo analyses of radial spoke transport, assembly, repair and maintenance. Cytoskeleton (Hoboken) 75, 352–362.

Lin J, Heuser T, Carbajal-Gonzalez BI, Song K, Nicastro D (2012). The structural heterogeneity of radial spokes in cilia and flagella is conserved. Cytoskeleton (Hoboken) 69, 88–100.

Lin J, Yin W, Smith MC, Song K, Leigh MW, Zariwala MA, Knowles MR, Ostrowski LE, Nicastro D (2014). Cryo-electron tomography reveals ciliary defects underlying human RSPH1 primary ciliary dyskinesia. Nat Commun 5, 5727.
Lucic V, Rigort A, Baumeister W (2013). Cryo-electron tomography: the challenge of doing structural biology in situ. J Cell Biol 202, 407–419.
Luck D, Piperno G, Ramanis Z, Huang B (1977). Flagellar mutants of Chlamydomonas: studies of radial spoke-defective strains by dikaryon and revertant analysis. Proc Natl Acad Sci USA 74, 3456–3460.
Luo W, Ruba A, Takao D, Zweifel LP, Lim RYH, Verhey KJ, Yang W (2017). Axonemal lumen dominates cytosolic protein diffusion inside the primary cilium. Sci Rep 7, 15793.
Maheshwari A, Obbineni JM, Bui KH, Shibata K, Toyoshima YY, Ishikawa T (2015). α- and β-Tubulin lattice of the axonemal microtubule doublet and binding proteins revealed by single particle cryo-electron microscopy and tomography. Structure 23, 1584–1595.
Marshall WF, Rosenbaum JL (2001). Intraflagellar transport balances continuous turnover of outer doublet microtubules: implications for flagellar length control. J Cell Biol 155, 405–414.
Martin NC, Goodenough UW (1975). Gametic differentiation in *Chlamydomonas reinhardtii*. I. Production of gametes and their fine structure. J Cell Biol 67, 587–605.
Mastronarde DN (2005). Automated electron microscope tomography using robust prediction of specimen movements. J Struct Biol 152, 36–51.
Mayfield SP, Bennoun P, Rochaix JD (1987). Expression of the nuclear encoded OEE1 protein is required for oxygen evolution and stability of photosystem II particles in *Chlamydomonas reinhardtii*. EMBO J 6, 313–318.
McIntyre JC, Williams CL, Martens JR (2013). Smelling the roses and seeing the light: gene therapy for ciliopathies. Trends Biotechnol 31, 355–363.
McVittie A (1972). Flagellum mutants of *Chlamydomonas reinhardtii*. J Gen Microbiol 71, 525–540.
Mitchell BF, Pedersen LB, Feely M, Rosenbaum JL, Mitchell DR (2005). ATP production in *Chlamydomonas reinhardtii* flagella by glycolytic enzymes. Mol Biol Cell 16, 4509–4518.
Nakazawa Y, Ariyoshi T, Noga A, Kamiya R, Hirono M (2014). Space-dependent formation of central pair microtubules and their interactions with radial spokes. PLoS One 9, e110513.
Obbineni JM, Yamamoto R, Ishikawa T (2017). A simple and fast approach for missing-wedge invariant classification of subtomograms extracted from filamentous structures. J Struct Biol 197, 145–154.
Oda T, Yanagisawa H, Yagi T, Kikkawa M (2014). Mechanosignaling between central apparatus and radial spokes controls axonemal dynein activity. J Cell Biol 204, 807–819.
Pandit S, Paul S, Zhang L, Chen M, Durbin N, Harrison SM, Rymond BC (2009). Spp382p interacts with multiple yeast splicing factors, including possible regulators of Prp43 DExD/H-Box protein function. Genetics 183, 195–206.
Patel-King RS, Gorbatyuk O, Takebe S, King SM (2004). Flagellar radial spokes contain a Ca^{2+}-stimulated nucleoside diphosphate kinase. Mol Biol Cell 15, 3891–3902.
Pazour GJ, Agrin N, Leszyk J, Witman GB (2005). Proteomic analysis of a eukaryotic cilium. J Cell Biol 170, 103–113.
Pedersen LB (2016). Tubulin transport in cilia: how many tubulin cargo-binding sites per IFT particle? (retrospective on DOI 10.1002/bies.201400007). Bioessays 39, 1.
Perales-Calvo J, Muga A, Moro F (2010). Role of DnaJ G/F-rich domain in conformational recognition and binding of protein substrates. J Biol Chem 285, 34231–34239.
Pettersen EF, Goddard TD, Huang CC, Couch GS, Greenblatt DM, Meng EC, Ferrin TE (2004). UCSF Chimera—a visualization system for exploratory research and analysis. J Comput Chem 25, 1605–1612.
Pigino G, Bui KH, Maheshwari A, Lupetti P, Diener D, Ishikawa T (2011). Cryoelectron tomography of radial spokes in cilia and flagella. J Cell Biol 195, 673–687.
Piperno G, Mead K, Henderson S (1996). Inner dynein arms but not outer dynein arms require the activity of kinesin homologue protein KHP1(FLA10) to reach the distal part of flagella in *Chlamydomonas*. J Cell Biol 133, 371–379.
Qin H, Diener DR, Geimer S, Cole DG, Rosenbaum JL (2004). Intraflagellar transport (IFT) cargo: IFT transports flagellar precursors to the tip and turnover products to the cell body. J Cell Biol 164, 255–266.
Rasala BA, Barrera DJ, Ng J, Plucinak TM, Rosenberg JN, Weeks DP, Oyler GA, Peterson TC, Haerizadeh F, Mayfield SP (2013). Expanding the spectral palette of fluorescent proteins for the green microalga *Chlamydomonas reinhardtii*. Plant J 74, 545–556.
Rezabkova L, Kraatz SH, Akhmanova A, Steinmetz MO, Kammerer RA (2016). Biophysical and structural characterization of the centriolar protein Cep104 interaction network. J Biol Chem 291, 18496–18504.
Rosenbaum JL, Child FM (1967). Flagellar regeneration in protozoan flagellates. J Cell Biol 34, 345–364.
Rosenbaum JL, Witman GB (2002). Intraflagellar transport. Nat Rev Mol Cell Biol 3, 813–825.
Rual JF, Venkatesan K, Hao T, Hirozane-Kishikawa T, Dricot A, Li N, Berriz GF, Gibbons FD, Dreze M, Ayivi-Guedehoussou N, *et al*. (2005). Towards a proteome-scale map of the human protein–protein interaction network. Nature 437, 1173–1178.
Satouh Y, Padma P, Toda T, Satoh N, Ide H, Inaba K (2005). Molecular characterization of radial spoke subcomplex containing radial spoke protein 3 and heat shock protein 40 in sperm flagella of the ascidian *Ciona intestinalis*. Mol Biol Cell 16, 626–636.
Schuck P (2003). On the analysis of protein self-association by sedimentation velocity analytical ultracentrifugation. Anal Biochem 320, 104–124.
Silflow CD, Sun X, Haas NA, Foley JW, Lefebvre PA (2011). The Hsp70 and Hsp40 chaperones influence microtubule stability in *Chlamydomonas*. Genetics 189, 1249–1260.
Sivadas P, Dienes JM, St Maurice M, Meek WD, Yang P (2012). A flagellar A-kinase anchoring protein with two amphipathic helices forms a structural scaffold in the radial spoke complex. J Cell Biol 199, 639–651.
Suzuki H, Noguchi S, Arakawa H, Tokida T, Hashimoto M, Satow Y (2010). Peptide-binding sites as revealed by the crystal structures of the human Hsp40 Hdj1 C-terminal domain in complex with the octapeptide from human Hsp70. Biochemistry 49, 8577–8584.
Tremblay V, Zhang P, Chaturvedi CP, Thornton J, Brunzelle JS, Skiniotis G, Shilatifard A, Brand M, Couture JF (2014). Molecular basis for DPY-30 association to COMPASS-like and NURF complexes. Structure 22, 1821–1830.
Wang X, Lou Z, Dong X, Yang W, Peng Y, Yin B, Gong Y, Yuan J, Zhou W, Bartlam M, *et al*. (2009). Crystal structure of the C-terminal domain of human DPY-30-like protein: a component of the histone methyltransferase complex. J Mol Biol 390, 530–537.
Wei M, Sivadas P, Owen HA, Mitchell DR, Yang P (2010). *Chlamydomonas* mutants display reversible deficiencies in flagellar beating and axonemal assembly. Cytoskeleton (Hoboken) 67, 71–80.
Yan W, Craig EA (1999). The glycine-phenylalanine-rich region determines the specificity of the yeast Hsp40 Sis1. Mol Cell Biol 19, 7751–7758.
Yang C, Compton MM, Yang P (2005). Dimeric novel HSP40 is incorporated into the radial spoke complex during the assembly process in flagella. Mol Biol Cell 16, 637–648.
Yang C, Owen HA, Yang P (2008). Dimeric heat shock protein 40 binds radial spokes for generating coupled power strokes and recovery strokes of 9 + 2 flagella. J Cell Biol 180, 403–415.
Yang P, Diener DR, Rosenbaum JL, Sale WS (2001). Localization of calmodulin and dynein light chain LC8 in flagellar radial spokes. J Cell Biol 153, 1315–1326.
Yang P, Diener DR, Yang C, Kohno T, Pazour GJ, Dienes JM, Agrin NS, King SM, Sale WS, Kamiya R, *et al*. (2006). Radial spoke proteins of Chlamydomonas flagella. J Cell Sci 119, 1165–1174.
Yang P, Yang C, Sale WS (2004). Flagellar radial spoke protein 2 is a calmodulin binding protein required for motility in *Chlamydomonas reinhardtii*. Eukaryot Cell 3, 72–81.
Ye F, Breslow DK, Koslover EF, Spakowitz AJ, Nelson WJ, Nachury MV (2013). Single molecule imaging reveals a major role for diffusion in the exploration of ciliary space by signaling receptors. Elife 2, e00654.
Zhu X, Liu Y, Yang P (2017a). Radial spokes—a snapshot of the motility regulation, assembly, and evolution of cilia and flagella. Cold Spring Harb Perspect Biol 9, 57–70.
Zhu X, Poghosyan E, Gopal R, Liu Y, Ciruelas KS, Maizy Y, Diener DR, King SM, Ishikawa T, Yang P (2017b). General and specific promotions of flagellar assembly by a flagellar nucleoside diphosphate kinase. Mol Biol Cell 28, 3029–3042.